□□□□□□□□□ □□□□□□□□□ □□□□□□ □
□□□□□□□□□□□□□ □□□□□□□ □□ □ □□□
□□□□□□□□

| | |
|---|---|
| □□□□□□ | □□ □□□□□□ □□□□□□ □□□□□□□□□□ □□ □□□□□□□□□ □□□ □□ □□□□□ □□ □□ □□□ |
| □□□□□□□ □□ □□□□□□□□□□□ □□□□□ | □□□□□□□ □□□□□□ □□□□□□ |
| □□□□□□ | □□□ |
| □□□□□□ | □□ |
| □□□□ □□□□□ | □□□□□□ |
| □□□□ | □□□□□□□□□□□ |
| □□□□□□□□□□ | □□□ □□□□□□□□□□ |
| □□□□□□ | □□□ □□□□ □□□ □□□□□□□□□□<br>□□□□ □□□□□□□ □□□ □□ □□□□□□□□□ □□□ □□□□□□□<br>□□□ □□□□□ □□□ □□□□□ □□□ □□□□□□□ □□□□□<br>□□□□□□□□□□ □□ □□□ □□□□□□ □□□ □□□ □□□□□□□□□□<br>□□□□ □□□□□□□ □□□□□□□ □□ □□□□□□ □□□□□□<br>□□□□□□□ □□□□□□□□□□□□□□ □□□ □□□ □□ □□□□□ □□<br>□□□□□□□□□□□□□□□□□□□□□□□□□□□□□□□□□□□□□□□□□□<br>□□□□□□□□ |
| □□□□□□□□□ □□□□ | □□□□□□ |
| □□□ | □□□□□□□□□□□□□□□□□□□□□□□□□□□□□□□□□□□□□□□□□ |

# Substrate stiffness affects particle distribution pattern in a drying suspension droplet

R. Iqbal[1], Atsushi Matsumoto[2], A. Sudeepthi[1], Amy Q. Shen[2], A. K. Sen[1,*]

[1]Microfluidics Laboratory, Dept. of Mechanical Engineering, Indian Institute of Technology Madras, Chennai, India, 600036
[2]Micro/Bio/Nanofluidics Unit, Okinawa Institute of Science and Technology Graduate University, Okinawa, Japan, 904-0412

The complexities involved to achieve tailor-made evaporative deposition pattern has remained a challenge. Here, we show that the morphological pattern of drying suspension droplets can be altered by varying substrate elastic modulus $E$. We find the particle spot diameter and spacing between the particles scale with substrate stiffness as $d_s \sim E^{-0.15}$ and $s \sim E^{-1.23}$, respectively. We show that the larger spot diameter and spacing between particles on a softer substrate is attributed to a higher energy barrier $U$ associated with stronger pinning of the contact line. The particle deposition pattern is characterized in terms of deposition index, $I_d$, whose value is $< 0.50$ and $> 0.75$ for centralized (multilayer) and uniform (monolayer) deposition patterns observed for stiffer and softer substrates, respectively. The outcome of the present study may find applications in biochemical characterization and analysis of micro/nano particles.

Droplet evaporation, apart from the association with the natural processes such as rain, fog and dew, has found applications in inkjet printing[1], spray cooling[2], DNA microarrays[3], biochemical assays[4] and spraying of pesticides[5] etc. The topic has been extensively studied over the past two decades giving rise to important scientific advancements and technological developments[6–9]. Evaporation of particulated droplets involves rich physicochemical phenomena such as particle/particle interaction, particle/substrate interaction, patterning and wetting. The seminal work by Deegan et al.[10] illustrated that an outwardly driven flow resulting from the differential evaporation flux drags micro/nano particles toward the three-phase contact line, which gives rise to the accumulation of particles in the form of a ring; famously known as "the coffee-ring effect".

The coffee ring effect has been exploited in various applications such as detection of malaria and other biomarkers[11,12], nanochromatography[13] and disease diagnostics[14]. On the contrary, the performance of the matrix assisted laser deposition ionization spectrometry (MALDI)[15], surface enhanced Raman spectroscopy (SERS)[16], fluorescent microarrays[17], and color filters in LCDs[18] are greatly hampered by this effect. Thus an in-depth understanding of the kinetics of evaporation and the subsequent morphological pattern would have utmost importance for such applications. By varying the physicochemical parameters such as ambient pressure[19], substrate temperature[20,21], relative humidity[22], substrate wettability[23], properties of the solute (shape, size and wettability)[24] and solvents (pH)[25], presence of the surfactants[26] and additives[27] and external flow fields[28,29], the evaporation kinetics and hence the resulting deposition pattern can be controlled. However, the above strategies are either intrusive (e.g. use of additives and surfactants) or involve complicated procedures (compromising the shape of solute particles, or composition of the liquid droplets) or external fields (i.e., electrowetting, acoustowetting).

While particles of a drying suspension droplet form coffee-ring patterns on hydrophilic substrates, they form centralized deposition patterns on hydrophobic substrates [21], both of which are undesirable for various applications. The goal of this work is to examine the effect of substrate stiffness on the centralized deposition pattern observed on a hydrophobic substrate. Recent studies have revealed some of the effects of viscoelastic properties of substrates on the evaporation kinetics and particle deposition pattern[30–32]. It was found that water droplets over a stiffer and a softer substrate evaporate with CCA (constant contact angle) and CCR (constant contact radius) mode respectively. Prolonged pinning and larger contact radius on a softer substrate led to faster evaporation. Moreover, a smaller receding contact angle and the faster contact line velocity was observed on a softer substrate. For example, 2 µm silica particles inside a water-silica suspension droplet displayed crater-like (centralized) deposits with no particles at the rim over a stiffer substrate; while straight necklaces were shown aligned toward the rim, over a softer substrate.

In the present work, we unravel the effect of substrate elasticity on the spot diameter and interdistance between particles. Using a theoretical model, we explain that in the case of softer substrates, observed larger spot diameter is attributed to a higher energy barrier; while larger interdistance between particles is attributed to the enhanced elastic deformation. Using polystyrene particles of different sizes and concentrations and different drop volumes, we show that for increasingly softer substrates, the spot diameter increases and a transition from a centralized and multilayer deposition pattern to an unexpected uniform and monolayer deposition pattern is observed. Such uniform and monolayer deposition pattern is difficult to achieve without direct compromise of liquid droplets (either by changing the shape of the microparticles or varying the pH of the solvents or adding the surfactants)[24-26]. Finally, we introduce a dimensionless parameter "deposition index ($I_d$)" in order to predict and control the centralized or the uniform deposition pattern. Our results suggests that, $I_d < 0.50$ results in a centralized (multilayer) deposition patterns over stiffer substrates; while $I_d > 0.75$ results in uniform (monolayer) deposition patterns over softer substrates.

The schematic of the experimental setup is shown in FIG. S1 (Section S1). Clean glass substrates (thickness ~ 1.1 mm, Matsunami, Japan) coated with a thin elastomeric layer (Sylgard 184, Dow Corning Toray, Japan) were used as the substrate for the experiments. To adjust elastic moduli of the substrate, crosslinkers were added to the base polymer at different ratios ranging from 10:1 to 50: 1 and the cross-linked substrates are herein after referred as P10, P20, P30, P40 and P50. The ratio of the base polymer to the crosslinkers and the corresponding elastic modulus of the substrates are presented in Table S1. We

1  performed experiments with suspension drops (DI water + polystyrene microparticles) of volume ranging $0.5 - 2.0$ μL
2  (maintaining $Bo << 1$) containing particles of size ranging $0.2 - 6$ μm at concentrations $10^8 - 10^9$ particles/mL, with
3  substrate contact angle of $113 \pm 10^o$ and stiffness in the range $E = 20 - 283$ kPa. For each experimental condition, identical
4  experiments were repeated at least five-times in order to establish the repeatability of the data and the error bars associated with
5  the data are estimated from the standard deviation of the data set. The materials and methods used for the fabrication of the
6  substrates of different elastic modulus, preparation of the microbeads at different concentrations and the experimental details
7  are outlined in SI (see section S1).

8  FIG.1a depicts top and side views of the dried suspension droplets (of volume 1.0 μL, particle size 1.0 μm, concentration
9  $10^9$ particles/mL) on the different substrates (P10, P30 and P50) of elastic modulus 283, 120 and 20 kPa respectively. The
10  initial contact radius (just after dispense) of the suspension droplet is indicated by the dotted line in the top views. In all cases,
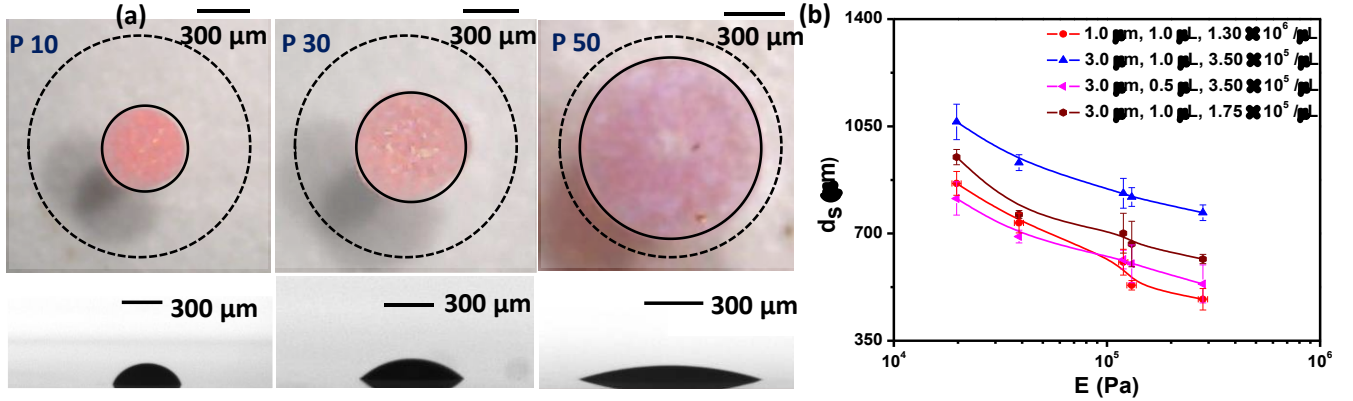


11
12  **FIG. 1.** (a) Differences in the morphological pattern (top & side views) of dried suspension droplets over P10 (E~283 kPa), P30 (E~120
13  kPa) and P50 (E~20 kPa) substrates. (b) Variation of the spot diameter, $d_s$ with the substrate elastic modulus, G for different droplet volume,
14  particle size and concentration.

15  owing to the hydrophobic nature of the substrates, instead of a coffee-ring, a centralized particle deposition pattern[23] is
16  observed. The spot size was obtained from the gray scale intensity plot shown in Fig S2a (Section S2). The diameter of the
17  dried particle spot was found to be much larger ($864 \pm 39$ μm) for substrates of lower elastic modulus (i.e. P50 with $E =$
18  20 kPa) as compared to that ($485 \pm 35$ μm) for a stiffer substrate (P10 with $E = 283$ kPa). FIG. 1b shows the variation of the
19  spot size with the substrate elastic modulus for different droplet volume, particle size and concentration (also see FIG. S3). As
20  observed, the particle spot diameter decreases with an increase in the substrate elastic modulus due to early receding of the
21  contact line owing to a smaller energy barrier, which is discussed later. From the experimental data, the spot diameter is
22  correlated with elastic modulus as $d_s \sim E^{-0.15}$ (with $R^2 = 0.95$).

23  In order to understand the contrasting morphological patterns on substrates of different elastic modulus, we looked into the
24  evaporation dynamics. The variation of the contact radius $\hat{r}$ $(r/r_o)$ and contact angle $\theta$ of drying suspension droplets (volume
25  1.0 μL, particle size 1 μm, concentration $10^9$ $particles/mL$) with time $\hat{t}$ $(t/t_E)$ on substrates of different elastic modulus $E =$
26  $20 - 283$ kPa) is shown in FIG. 2a and S4a in SI. The contact radius $r$ is normalized with respect to the initial contact radius
27  $r_0$ (i.e. $\hat{r} = r/r_0$) and timescale t is normalized with respect to the corresponding evaporation time scale $t_E$ (i.e. $\hat{t} = t/t_E$).

28  We observe that compared to a rigid substrate ($\hat{t}_p = 0.36$, $E = 283$ kPa), a droplet remains pinned over a much longer time
29  ($\hat{t}_p = 0.94$) on a softer substrate, where $\hat{t}_p$ is the dimensionless timescale over which the contact line remains pinned. Since
30  the contact line of a droplet remains pinned over a prolonged period of time on a softer substrate, the evaporation timescale $t_E$
31  (which is inversely proportional to the contact radius[32]) was found to be lower for smaller substrate stiffness (see FIG.2b). From
32  FIG. 2a, over a timescale $t < \hat{t}_p$ , when the contact line remains pinned, the contact angle decreases continuously and approach
33  the receding contact angle $\theta_r$. For $\hat{t} > \hat{t}_p$ , the contact line either recedes with a constant contact angle or both the contact radius
34  and contact angle decrease simultaneously exhibiting a mixed mode of evaporation. The variation of receding contact angle $\theta_r$,
35  with substrate elastic modulus $E$ is also depicted in FIG. 2b which shows that the receding angle $\theta_r$ scales with substrates
36  elastic modulus $E$ following $\theta_r \sim E^{0.20}$ (with $R^2 = 0.86$ ).
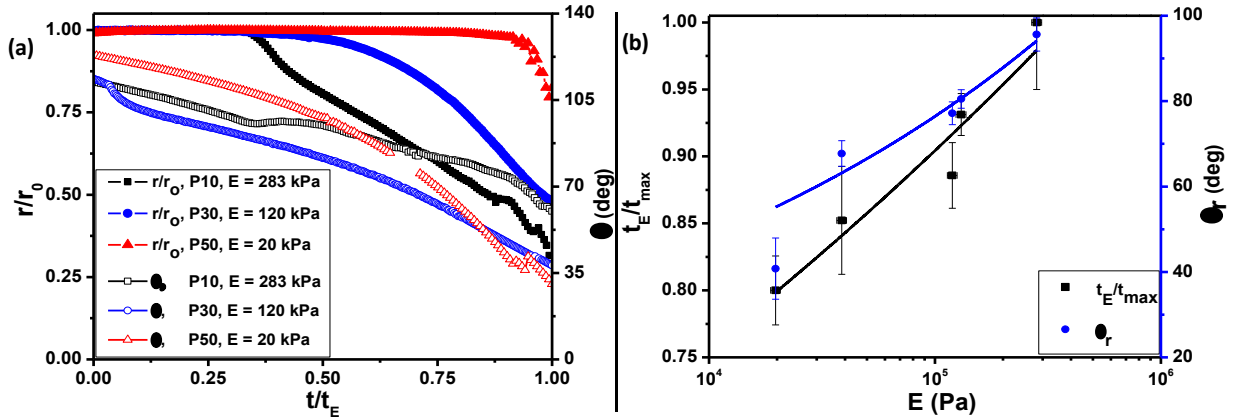
**FIG. 2.** (a) Variation of normalized contact radius ($\hat{r} = r/r_0$) and contact angle ($\theta$) over substrates of different elastic modulus: P10 ($E \sim 283\ kPa$), P30 ($E \sim 120\ kPa$) and P50 ($E \sim 20\ kPa$) respectively. (b) Variation in the normalized evaporation timescale and the receding contact angle with the substrate elastic modulus, $E$.

We see that in case of a stiffer substrate ($E = 283$ kPa), the contact line recedes early ($\hat{t}_p = 0.36$) thus carrying the particles towards the center of the droplet giving rise to a much smaller particle spot diameter ($485\ \mu m$) and particle deposition over multiple layers. On the other hand, in case of a softer substrate ($E = 20$ kPa), pinning of the contact line over a significant part of the evaporation timescale ($\hat{t}_p = 0.94$) prevents migration of the particles towards the center resulting in a much larger spot diameter (i.e. $863\ \mu m$) with distribution of particles in the form of a monolayer. Next, we employ a theoretical model to explain the above phenomena from the argument of free energy.

Droplets with Bond number, $Bo \ll 1$, take the shape of a spherical cap (FIG. 3a) due to the absence of the gravimetric flattening and in that case the droplet volume $V$ and liquid/vapor interfacial area $A$ can be expressed as

$$V = \frac{\pi r^3}{3 sin^3\theta}(1 - cos\theta)^2(2 + cos\theta), \ \ A = \frac{2\pi r^2}{(1 + cos\theta)} \tag{1}$$

where, $r$ and $\theta$ are respectively the contact radius and the contact angle of the droplet on a real surface. The Gibbs free energy $G_b$ of the droplet arising from the interfacial energy components can be written as $G_b = \gamma_{LV}A + \pi r^2(\gamma_{SL} - \gamma_{SV})$, where $\gamma_{LV}, \gamma_{SL}$ and $\gamma_{SV}$ are the liquid-vapor, solid-liquid and solid-vapor interfacial tension values. Using expression for the interfacial area from equation (1), we get

$$G_b = \gamma\pi r^2 \left[\frac{2}{(1 + cos\theta)} - cos\theta_o\right] \tag{2}$$

where $\theta_o$ is the equilibrium contact angle of the droplet obtained from the Young's equation. Unlike an ideal surface, the droplet on a real/non-ideal surface remains out of equilibrium due to surface asperities and chemical inhomogeneity[33]. Let the droplet be perturbed from its equilibrium state such that the modified contact radius becomes $r = r_o + \delta r$ and accordingly the corresponding contact angle is $\theta = \theta_o - \delta\theta$, where $r_o$ is the equilibrium contact radius (see Fig 3a). On an ideal surface, the contact angle of a liquid droplet corresponds to the Young's contact angle which remains constant and the contact radius decreases during droplet evaporation. However, on a soft substrate, the surface asperities, (see supplementary section S6) chemical inhomogeneity and more importantly the wetting ridge[34,35] together would offer an energy barrier $U$ that prevents smooth receding of the contact line which remains pinned and only contact angle decreases.
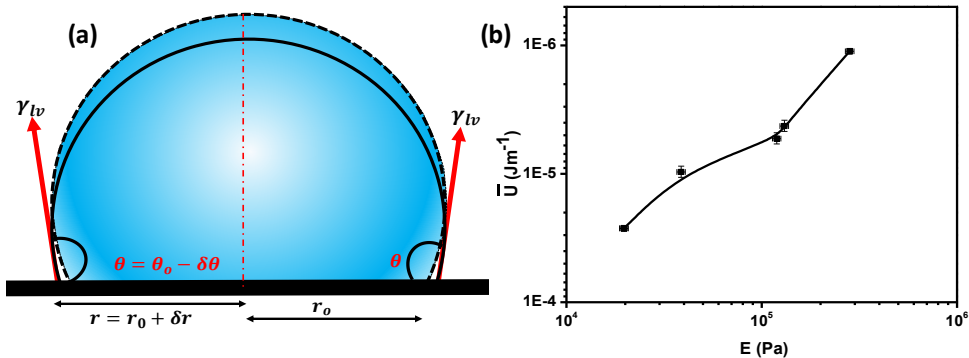


**FIG.3.** (a) A schematic of the droplet over a hydrophobic substrate. The droplet over ideal and non-ideal surface is denoted by the dotted and the solid line respectively. (b) Variation of the potential energy barrier (per unit length), $\bar{U}$, with the substrate elastic modulus.

With the progress in evaporation, the volume of the droplet decreases and thus for a droplet pinned at the contact line, the contact angle decreases. This leads to a lack in capillary equilibrium and the absence of capillary equilibrium is the source of excess free energy. Free energy of the non-equilibrated droplet can be obtained from the Taylor series expansion (and using the condition that droplet is at equilibrium at $r = r_o$, thus $\left(\frac{dG_b}{dr}\right)_{r=r_o} = 0$ and constant droplet volume $dV = 0$) as:

$$\delta G_b \cong \left(\frac{d^2 G_b}{dr^2}\right)_{r=r_o} \frac{(\delta r)^2}{2} \cong \frac{2\pi r^2 \gamma_{LV}(\delta\theta)^2}{2(2+\cos\theta_o)} \qquad (3)$$

where $\delta\theta$ is the differences between the actual contact angle (from the experiments, that decreases for a pinned droplet with the reduction in the volume during evaporation), and the corresponding equilibrium value $\theta_o$. Taking $\theta_a$ as the actual contact angle at any time instant, we can write $\delta\theta = (\theta_o - \theta_a(t))$. Thus, we get

$$\delta G_b\,(t) \cong \left(\frac{d^2 G_b}{dr^2}\right)_{r=r_o} \frac{(\delta r)^2}{2} \cong \frac{2\pi r^2 \gamma_{LV}(\theta_o - \theta_a(t))^2}{2(2+\cos\theta_o)} \qquad (4)$$

During the evaporation process, the actual contact angle $\theta_a$ decreases as time progresses and thus the excess Gibbs free energy $\delta G_b$ increases with time. The variation in the excess Gibbs free energy $\delta G_b$ with the actual contact angle $\theta_a$, which is a function of time $t$, for different substrate stiffness, is shown in FIG. S5. As observed, when the contact angle attains the receding contact angle $\theta_r$, the excess Gibbs free energy attains the maximum value i.e. $\delta G_{max}$, which overcomes the energy barrier $U$ and the contact line recedes. Using the previous equation, the maximum excess Gibbs free energy per unit length of the contact line $\overline{\delta G_{max}}$ or, the energy barrier $\overline{U}$) is obtained as

$$\overline{U} = \overline{\delta G_{max}} = \frac{1}{2\pi r} \times \frac{2\pi r^2 \gamma_{LV}((\theta_o - \theta_r))^2}{2(2+\cos\theta_o)} \qquad (5)$$

From the above equation, we plot the variation of maximum excess free energy $\overline{\delta G_{max}}$ or, the energy barrier $\overline{U}$ with substrate elastic modulus $E$ (see FIG. 3b). As observed, the energy barrier $\overline{U}$ is higher for a softer substrate ($E = 20$ kPa) and thus the contact line remains pinned for a much longer duration of time $\hat{t}_p$ until the receding contact angle $\theta_r$ is attained. The higher energy barrier explains why a suspension droplet remains pinned for a longer time on a softer substrate yielding a more homogeneous particle distribution pattern.

SEM images of the morphological patterns of the particles with substrates of elastic modulus 283 kPa and 20 kPa are depicted in FIG. 4a (also see in FIG. S6a and FIG. S6b), respectively. As observed, in the case of a rigid substrate, particles get deposited in a closed pack multiple layers whereas a loosely packed, homogeneous, uniform monolayer particle deposition is observed in the case of a softer substrate. Also, in contrast to the rigid substrate in which the particles are packed closely, the interdistance ($s$) between the particles is found to be higher in the case of a softer substrate ($E = 20$ kPa) as compared to that for a stiffer substrate ($E = 283$ kPa). The hexagonal polygons obtained from the voronoi diagram[36] for both substrates (inset of FIG. 4a and FIG.S6) shows the ordered arrangements of the particles. In the case of the stiffer substrate, apart from the hexagonal polygons, other polygons in square, rhombohedral and random shapes lead to the disorderliness in the pattern. The optical profilometry results (see FIG. S7) suggest a disk-like pattern and uniform pattern for the stiffer and softer substrates, respectively. The variation in the interparticle distance ($s$) with substrate elastic modulus $E$ for different particle sizes is presented in FIG. 4b. From the data, interparticle distance correlates with the substrate elastic modulus as $s \sim E^{-1.23}$.
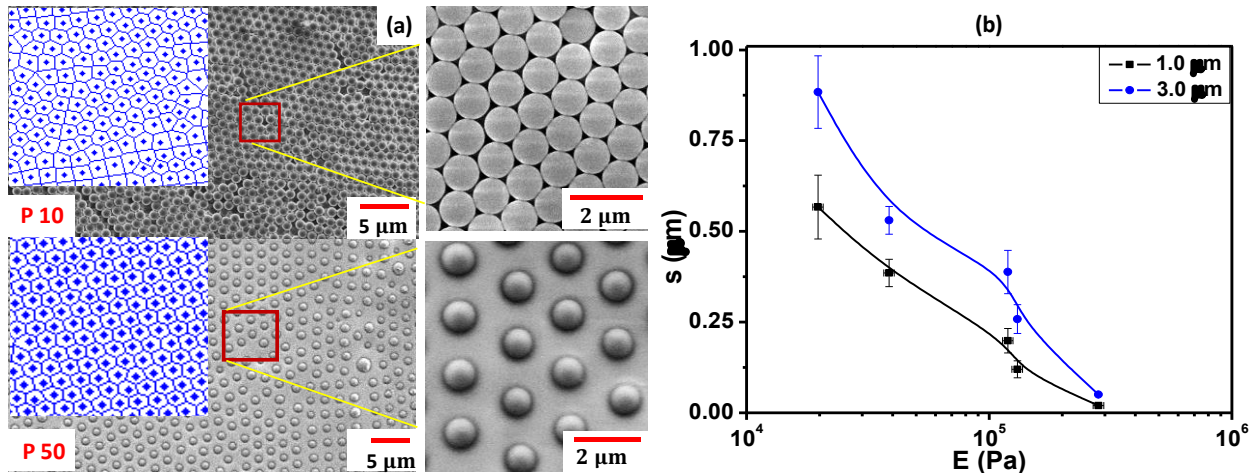


FIG. 4. (a) Differences in the morphological pattern obtained under SEM for (a) stiffer ($E \sim 283$ kPa) and softer ($E \sim 20$kPa) substrate, particle size 1μm, (b) Variation of the interparticle distance ($s$), with the substrate elastic modulus, $E$ for two different particle size, 1 and 3 μm respectively.

1    For an evaporative suspension droplet, to predict and control either the formation of a multi-layer centralized deposition pattern
2    or the formation of a uniform monolayer deposition pattern, we investigated the influence of the suspension droplet volume
3    ($V$), size and concentration of the microparticles ($a$ and $C$), surface tension ($\gamma$) and the elastic modulus ($E$) on the evaporative
4    deposition pattern of the suspension droplet. We introduced a dimensionless parameter (see the section S5 in SI), "deposition

5    index" $I_d = \dfrac{0.33a(CV)^{0.54}(\frac{\gamma}{Ea})^{0.21}}{[(8/\pi)Vf(\theta)]^{\frac{1}{3}}}$, which is the ratio of the final deposition contact diameter after the complete evaporation of the

6    droplet to the initial (maximum) contact diameter of the droplet when dispensed, where $f(\theta) = \dfrac{3sin^3\theta}{[(1-cos\theta)^2(2+cos\theta)]}$ is indicative
7    of the contribution of the contact angle on the volume of the spherical cap. The initial contact line diameter is obtained from
8    equation 1 and the numerator is obtained from fitting of the data presented in FIG. 1b and FIG. S3. With a very diluted
9    suspension droplet, a monolayer along with centralized deposition pattern can also be achieved due to the lack of the adequate
10    number of particles. Thus, to achieve a uniform and a monolayer deposition pattern, the particles concentration (numbers per

11    unit volume) should be of the order of a critical value given as: $C_{crit} \sim \dfrac{P.F[2.5Vf(\theta)]^{\frac{2}{3}}}{a^2V}$, where P.F is the maximum packing fraction.
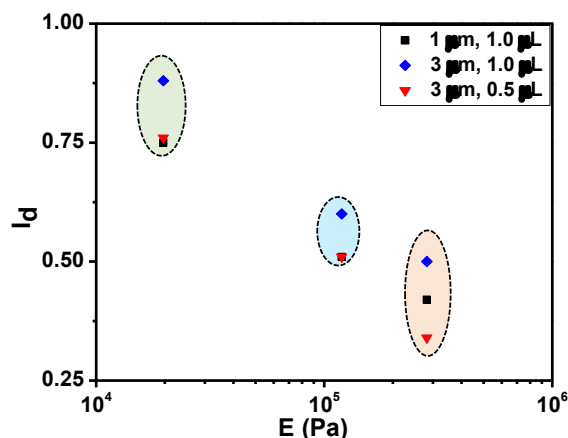


12

13    **FIG. 5.** Variation of deposition index, $I_d$, with $E$ for different particle size and droplet volume.

14    Figure 5 depicts the variation of $I_d$ with $E$, for different particle size and droplet volume. It is observed that for a particle size
15    of 1 μm and concentration $10^6/\mu L$ presented in the FIG. 2a, the value of $I_d$ is calculated to be 0.41 for the P10 and 0.75 for
16    the P50 substrates, in agreement with the non-uniform (and multilayers) and uniform (and monolayer) deposition patterns
17    observed in the case of P10 and P50 substrates respectively. It can be observed that in order to obtain a uniform deposition
18    pattern, the deposition index $I_d \sim 0.75 - 0.85$, whereas $I_d \sim 0.25 - 0.50$ would yield a non-uniform deposition pattern. Thus,
19    to obtain best results in characterization and analysis of particles for biological and analytical applications, with other
20    parameters fixed, substrate stiffness should be chosen judiciously to ensure large values of $I_d$ .

21    In summary, we reported the role of substrate elastic modulus on the particle distribution pattern in a drying suspension droplet.
22    We observed that the particle spot diameter and interparticle distance can be controlled by simply varying the substrate elastic
23    modulus. The outcome of the present study is relevant for ensuring a uniform and monolayer particle deposition pattern for the
24    characterization and analysis of microparticles via analytical techniques.

25    See the supplementary information for the experimental details, rheological characterization, detailed evaporation kinetics
26    morphological patterns under SEM and optical profilometry.

35    **References**
36    [1] B.-J. de Gans and U.S. Schubert, Langmuir **20**, 7789 (2004).
37    [2] C. Wang, R. Xu, Y. Song, and P. Jiang, Int. J. Heat Mass Transf. **112**, 279 (2017).
38    [3] M. Schena, D. Shalon, R.W. Davis, and P.O. Brown, Science (80-. ). **270**, 467 (1995).
39    [4] S. Weidner, P. Knappe, and U. Panne, Anal. Bioanal. Chem. **401**, 127 (2011).

5 Y. Yu, H. Zhu, J.M. Frantz, M.E. Reding, K.C. Chan, and H.E. Ozkan, Biosyst. Eng. **104**, 324 (2009).

6 H. Hu and R.G. Larson, J. Phys. Chem. B **106**, 1334 (2002).

7 A.-M. Cazabat and G. Guéna, Soft Matter **6**, 2591 (2010).

8 H.Y. Erbil, Adv. Colloid Interface Sci. **170**, 67 (2012).

9 D. Brutin and V. Starov, Chem. Soc. Rev. **47**, 558 (2018).

10 R.D. Deegan, O. Bakajin, T.F. Dupont, G. Huber, S.R. Nagel, and T.A. Witten, Nature **389**, 827 (1997).

11 J.R. Trantum, D.W. Wright, and F.R. Haselton, Langmuir **28**, 2187 (2012).

12 J.T. Wen, C.-M. Ho, and P.B. Lillehoj, Langmuir **29**, 8440 (2013).

13 T.-S. Wong, T.-H. Chen, X. Shen, and C.-M. Ho, Anal. Chem. **83**, 1871 (2011).

14 D. Brutin, B. Sobac, B. Loquet, and J. Sampol, J. Fluid Mech. **667**, 85 (2011).

15 O. Kudina, B. Eral, and F. Mugele, Anal. Chem. **88**, 4669 (2016).

16 W. Wang, Y. Yin, Z. Tan, and J. Liu, Nanoscale **6**, 9588 (2014).

17 R. Blossey, A. Bosio, Langmuir **18**, 2952 (2002).

18 Y.-C. Lin, Y.-Y. Lin, D.S.H. Wong, T.-J. Liu, S.-H. Wen, and K.-T. Huang, J. Appl. Polym. Sci. **120**, 1555 (2011).

19 A. Askounis, K. Sefiane, V. Koutsos, and M.E.R. Shanahan, Colloids Surfaces A Physicochem. Eng. Asp. **441**, 855 (2014).

20 M. Parsa, S. Harmand, K. Sefiane, M. Bigerelle, and R. Deltombe, Langmuir **31**, 3354 (2015).

21 N.D. Patil, P.G. Bange, R. Bhardwaj, and A. Sharma, Langmuir **32**, 11958 (2016).

22 V.H. Chhasatia, A.S. Joshi, and Y. Sun, Appl. Phys. Lett. **97**, 231909 (2010).

23 R. Iqbal, B. Majhy, A.Q. Shen, and A.K. Sen, Soft Matter **14**, 9901 (2018).

24 P.J. Yunker, T. Still, M.A. Lohr, and A.G. Yodh, Nature **476**, 308 (2011).

25 R. Bhardwaj, X. Fang, P. Somasundaran, and D. Attinger, Langmuir **26**, 7833 (2010).

26 T. Still, P.J. Yunker, and A.G. Yodh, Langmuir **28**, 4984 (2012).

27 L. Cui, J. Zhang, X. Zhang, L. Huang, Z. Wang, Y. Li, H. Gao, S. Zhu, T. Wang, and B. Yang, ACS Appl. Mater. Interfaces **4**, 2775 (2012).

28 D. Mampallil, J. Reboud, R. Wilson, D. Wylie, D.R. Klug, and J.M. Cooper, Soft Matter **11**, 7207 (2015).

29 H.B. Eral, D.M. Augustine, M.H.G. Duits, and F. Mugele, Soft Matter **7**, 4954 (2011).

30 Y.S. Yu, Z.Q. Wang, and Y.P. Zhao, Acta Mech. Sin. **29**,799 (2013).

31 M.C. Lopes and E. Bonaccurso, Soft Matter **9**, 7942 (2013).

32 M.C. Lopes and E. Bonaccurso, Soft Matter **8**, 7875 (2012).

33 M. Oksuz and H.Y. Erbil, J. Phys. Chem. C **118**, 9228 (2014).

34 S.J. Park, B.M. Weon, J.S. Lee, J. Lee, J. Kim, and J.H. Je, Nat. Commun. **5**, 4369 (2014).

35 A. Carre and M.E.R. Shanahan, Langmuir **11**, 3572 (1995).

36 Á.G. Marín, H. Gelderblom, D. Lohse, and J.H. Snoeijer, Phys. Rev. Lett. **107**, 085502 (2011).